Hindawi
Journal of Nanotechnology
Volume 2019, Article ID 4628765, 19 pages
https://doi.org/10.1155/2019/4628765

Research Article

Optimization of Working Conditions for Perovskite-Based Gas Sensor Devices by Multiregression Analysis

Fabio Zaza,[1] **Vanessa Pallozzi**,[2] **and Emanuele Serra**[1]

[1]*ENEA-Casaccia Research Centre, Via Anguillarese 301, 00123 Rome, Italy*
[2]*Tuscia University, Via S. Camillo de Lellis, 01100 Viterbo, Italy*

Correspondence should be addressed to Fabio Zaza; fabio.zaza@enea.it

Received 21 August 2018; Revised 21 November 2018; Accepted 2 December 2018; Published 20 January 2019

Academic Editor: Eduard Llobet

Environmental degradation and resource depletion drive scientific research priorities to develop technologies for sustainable productive systems. Among them, chemical sensing technology plays a key role for regulating energetic, ecological, and productive efficiency by monitoring and controlling the industrial processes. Semiconducting metal oxide sensors are particularly attractive technology because of their simplicity in function, small size, and projected low cost. The aim of this work is to synthesize Ti-substituted lanthanum ferrite perovskite, $LaFe_{0.8}Ti_{0.2}O_3$, in order to develop a resistive sensor device for monitoring carbon monoxide. Since sensor performances are affected by experimental factors, such as temperature, target gas concentration, and gas flow rate, the aim of the authors was to define the optimum working condition by performing multiple regression analyses. The investigated ranges of operating conditions were temperature from 300 to 480°C, carbon monoxide concentration from 100 to 200 ppm, and inlet-gas flow rate from 40 to 100 cm^3/min. The results confirm that the applied systematic analysis is a powerful method for studying the direct and indirect effects of every experimental factor on sensor performance and for computing mathematical models with predictive ability, that are useful tools for defining the optimum chemiresistors' operating conditions. In addition, mathematical models are able to be used as multiple-factor surface calibration for restive gas sensor devices.

1. Introduction

The unsustainable management of industrial processes has been leading to global critic issues, concerning the depletion of energy and material natural resources and the degradation of the environment. This scenario drives scientific research priorities to develop technologies for sustainable productive systems in order to increase the process efficiency. Among these, nuclear and fuel cell are promising green power technologies, but they have open challenges yet, such as the issues related to the nuclear waste management [1] and fuel cell reliability [2], respectively. For these reasons, the research is currently focused on developing facilitative technologies to control the conventional unsustainable technology in order to convert it to a sustainable one. In this scenario, chemical sensing devices play a key role because they are used for monitoring the environmental impact of the industrial process, for checking the plant safety, and for controlling by feedback actions the productive system sustainability in order to improve the energetic, ecological, and productive efficiency [3–5].

Chemiresistors are attractive sensors because of their small dimensions, high sensitivity, fast response, simple structure and consequent easy fabrication, simplicity in function, and low cost [6, 7]. The sensing material is based on metal oxide semiconductors whose electrical resistance is affected by the presence of a target gas in the atmosphere. Indeed, reducing target gas, such as CO, subtracts the adsorbed oxygen from the metal oxide surface, leaving two free electrons and leading to either lower electrical resistance in n-type semiconductors or higher electrical resistance in p-type semiconductors. In order to have high-performance sensors with high sensitivity, response rate, and stability, the authors have synthesized sensing materials based on semiconductor metal oxide with two useful properties: dimensions at nanoscale and chemical nature highly stable,

right as perovskite-type oxides. The nanometric dimension improves the sensor performance, including sensitivity and response rate. Indeed, sensor sensitivity is high when the grain size is smaller than the Debye length because there is no electrical contribution of the bulk which otherwise masks the conductivity changes of the surface interacting with the target gas. Sensor response is fast when sensing material is nanostructured because the large surface area promotes the reaction rate between the target gas and the adsorbed oxygen [8–12]. Finally, the sensor reliability due to its signal stability is assured by using perovskite as a sensing material because this type of metal oxide has high chemical and thermal stability, preventing the sensor baseline drift due to aging effects under high temperature and target gas flowing.

Perovskite-type oxides have the general formula ABO_3, where the small B metal is placed inside the corner-sharing octahedra BO_6 that form a three-dimensional network with suitable interstices for the large cation A. Since almost all elements are stable in perovskite structure because of their suitable size and charge, a large number of compounds can be synthesized. For this reason, it is possible to design and synthesize perovskite oxides with the most suitable chemical composition and stoichiometry in order to develop sensing material for detecting specific target gas under specific working temperature [13, 14].

Perovskite oxides are solid ionic material that exhibit ionic, electronic, or mixed ionic-electronic conductivity, depending on the chemical stoichiometry, the working temperature, and the reducing/oxidizing atmosphere [15]. Since cationic vacancies are much less mobile than oxygen vacancies, the oxygen vacancies together with electrons and holes determine electrical properties of perovskites [16].

The concentration of oxygen vacancies depends on both the oxygen partial pressure and the temperature, according to the principle of Le Chatelier. Indeed, oxygen vacancies formation is promoted under high temperature and low oxygen partial pressure according to endothermic reaction (1), while oxygen vacancies refilling is promoted under low temperature and high oxygen partial pressure in agreement with the exothermic reaction (2) [17, 18]:

$$O_O^X \longrightarrow V_{\ddot{O}} + 2e^- + \frac{1}{2}O_{2(g)}, \quad (1)$$

$$\frac{1}{2}O_{2(g)} + V_{\ddot{O}} \longrightarrow O_O^X + 2h^+, \quad (2)$$

where O_O^X is oxygen with neutral charge sitting on the perovskite lattice site and $V_{\ddot{O}}$ is oxygen vacancy with double positive charge, following the Kroger–Vink notation. At the same time, oxygen vacancies formation leads to an increase in free-electron concentration, while oxygen vacancies refilling leads to an increase in free electronic-hole concentration: in other words, reactions (1) and (2) act as self-doping processes, where oxygen vacancy is a donor-dopant and oxygen is an acceptor-dopant. In addition, the concentration of both electron and holes depends on the energy bandgap and temperature because high temperature promotes electrons from the valence band to the conduction band [19].

The dependence of electronic conductivity on partial pressure of oxygen or, in general, the reducing/oxidizing gas is the working principle of resistive gas sensors. Under low oxygen pressure, the electrical conduction is mainly due to free electrons, n-type domain; while under high oxygen pressure it is mainly due to holes, p-type domain. Under intermediate oxygen pressure, if the energy bandgap is high enough to limit the concentration of free electrons and holes, the ion conduction of oxygen vacancies prevails the electronic conduction, ionic domain. Since ion conductivity does not change with oxygen pressure, semiconductor gas sensor has to work outside this domain [20]. Since $LaFeO_3$-based perovskite has low-energy bandgap between the valence band O_{2p} and the conduction band Fe_{3d} [21–23], it does not show ionic domain and it can work as resistive sensing material under any reducing/oxidizing pressure range [24, 25].

For this reason, the purpose of the authors is to design $LaFeO_3$-based perovskite for detecting carbon monoxide. Ti-substituted lanthanum ferrite perovskites, $LaFe_{0.8}Ti_{0.2}O_3$, have been synthesized and the effect of sensor operating conditions, such as target gas concentration, C, working temperature, T, and inlet-gas flow rate, φ, has been studied on the performances of the sensor device. Nanostructured perovskite oxides were obtained by means of the autocombustion method [26], which is a fast, easy, scalable, and reliable way for the synthesis of nanopowder. Since the sensor performance depends on multiple factors, whose effects can be both direct and indirect, chemometric analyses were executed in order to define the most useful operating condition for having sensor response with high quality, in agreement with the Quality-by-Design principles [27]. This analytical method includes both the choice of investigated factorial values for every test, following a systematic design of experiment, and the data elaboration by means of multiregression analysis in order to develop mathematical models with predictive ability.

2. Materials and Methods

2.1. Synthesis of Materials. $LaFe_{0.8}Ti_{0.2}O_3$ nanopowder, with controlled size and composition, was obtained by means of the autocombustion synthesis method. A reacting solution was prepared, where citrate ions were the fuel and the nitrate ions were the oxidizing agents. Metal ions were added in the right amount for having 0.35 g of perovskite oxide with the desired stoichiometry: 0.6348 g of lanthanum nitrate $La(NO_3)_3{\cdot}6H_2O$; 0.4786 g of iron nitrate $Fe(NO_3)_3{\cdot}9H_2O$; 0.1018 g of titanium butoxide $Ti(C_4H_9O)_4$. Since citrate ions act also as complexing agents, 1.5249 g of citric acid (CA), $C_6H_8O_7{\cdot}H_2O$, was added to have the right mole for assuring the complete complexation and subsequent dissolution of all metal ions. Since the added titanium salt has an organic component acting as a fuel, 2.8822 g of ammonium nitrate NH_4NO_3 was added in order to have fuel-to-oxidizer molar ratio close to the stoichiometric condition, by taking in account the molar amount of both citrate and butoxide ions. Finally, as much ammonium hydroxide (NH_4OH) as it is necessary to neutralize the solution acidity was added, because otherwise it prevents the citric acid dissociation into citrate anion, which is required for the complexation of

metal ions. The reacting solution was heated at 100°C under continuous stirring with a magnetic agitator until a dried dark gel was obtained. The dried gel was further heated at higher temperatures progressively. When the temperature of the heater was set at 200°C, which is the ignition temperature, the explosive reaction started, developing with a sharp self-acceleration. Actually, the reaction did not occur simultaneously and uniformly at all points of the sample because it started from hot spots, which were parts of the gel closer to the heater and with thinner thickness. For this reason, flame propagation was observed until all fuel was consumed and a fluffy powder was produced. The obtained powder was calcined in air at 600°C for 2 hours in order to complete the combustion of unburned or partially burned fuel, remove carbonaceous matter, and promote the crystallization of perovskite oxide.

2.2. Preparation of Sensor Devices. The powder of perovskite sensing material (Figure 1(a)) was mixed with organic solution, containing ethyl cellulose as binder, therpineol as high-boiling solvent, and isopropanol as low-boiling solvent, in order to obtain a viscous slurry ((Figure 1(b)) easy to deposit on the surface of sensing material holder (Figure 1(d)). The latter is a tile of alumina with two interdigitated gold electrodes (Figure 1(c)).

2.3. Characterization of Materials. The sample was analyzed by X-ray diffraction (XRD) technique in order to identify the phases and determine both the crystalline structure and the crystallite size. The analyses were performed by means of the Rigaku Miniflex diffractometer with Cu-Kα radiation, investigating the range $2\theta = 30^\circ$–80° with the scan rate 0.3°/min. The raw XRD data were mathematically elaborated by the Savitzky method for smoothing the pattern profile, with the Sonneveld method for defining the background and with the the Rachinger method for removing the false peaks due to the $K\alpha_2$ radiation.

The morphology of the synthesized powder was observed by means of the scanning electron microscopic (SEM) analysis. The microscope was Gemini LEO 1530 FEG-SEM by Zeiss with an acceleration voltage of Vacc = 0.2–30 kV and a resolution of 1.0 nm at 20 kV, 2.5 nm at 1 kV, and 5.0 nm at 0.2 kV.

2.4. Characterization of Sensors. The most useful parameters to compare the performances of sensor device are sensitivity, response time, resolution, and temporal stability [27–29]. The latter is defined as the response reliability, that depends on the signal drift and it is related to the electrical resistance changes in pure nitrogen atmosphere before and after flowing the target gas into the testing vessel.

Since the sensitivity toward CO is related to the sensor ability to detect the gas at a given concentration by changing electrical resistance, it is usually calculated the relative sensitivity, which is the ratio between the electrical resistance measured in pure nitrogen and in nitrogen containing the target gas CO. However, in order to remove the eventual drift and normalize the response, the authors calculate the fractional sensitivity FS [30], which is the ratio between the resistance changes due to the target gas effects and the resistance measured in pure nitrogen:

$$\mathrm{FS}(\%) = \frac{\left|R_{N_2}(\Omega) - R_{CO}(\Omega)\right|}{R_{N_2}(\Omega)} \cdot 100. \quad (3)$$

The response time is a typical parameter for kinetic performance evaluation, and it is defined as the time required to reach 90% of the maximum of the sensor output after applying the testing gas. However, it is not a reliable kinetic parameter because it is difficult to compare kinetic performance of different sensors by comparing directly and unequivocally different experimental response time values. Indeed, since the electrical resistance of high-sensitive sensor needs long time to reach the plateau value, the response time of high-sensitive and fast-responding sensor can have the same value as one of low-sensitive and slow-responding sensors. In other words, a sensor can take time to reach the plateau value not because it works slowly, but because it has high sensitivity. For this reason, the evaluation of kinetic performance is more conveniently done by comparing the response rate, defined as electrical resistance changes per unit of time. However, this parameter is not reliable as well because it is affected by the electrical resistance full scale. Indeed, the reaction rate of high-resistive, which means large full-scale, and high-sensitive sensor can have the same value as the one of low-resistive, which means small full-scale, and high-sensitive sensor. In other words, the sensor can have low reaction rate not because the resistance takes time to reach the steady sate condition, but because it works under small full scale. For this reason, the authors calculate the normalized response rate, rFS, that is obtained as the maximum fractional sensitivity changes per unit of time, corresponding to the slope of the fractional sensitivity profile at the flex point before reaching the plateau value:

$$\mathrm{rFS}\left(\%\mathrm{s}^{-1}\right) = \left[\frac{d\mathrm{FS}(\%)}{dt\,(s)}\right]_{(d^2\mathrm{FS}/dt^2)=0}. \quad (4)$$

The resolution is defined as the smallest change in a quantity being measured that causes a perceptible change in the corresponding indication [31]. Resistive sensor resolution depends on both the full scale and the output error because it is directly proportional to the electrical resistance span and inversely proportional to the electrical resistance standard deviation. In order to compare sensor performances under different experimental conditions, the authors define the resolution ability index, RAI, which is a useful normalized parameter for this purpose. This parameter is defined as the ratio between the span of fractional sensitivity and its pooled standard deviation:

$$\mathrm{RAI}(d.u.) = \frac{\Delta\mathrm{FS}(\%)}{\mathrm{sd}_{\mathrm{pooled}}(\%)}, \quad (5)$$

where ΔFS is the algebraic difference between the maximum and minimum fractional sensitivity values and $\mathrm{sd}_{\mathrm{pooled}}$ is the weighted average of the all individual standard deviations, assuming that all measurements have the same source of random error [32].

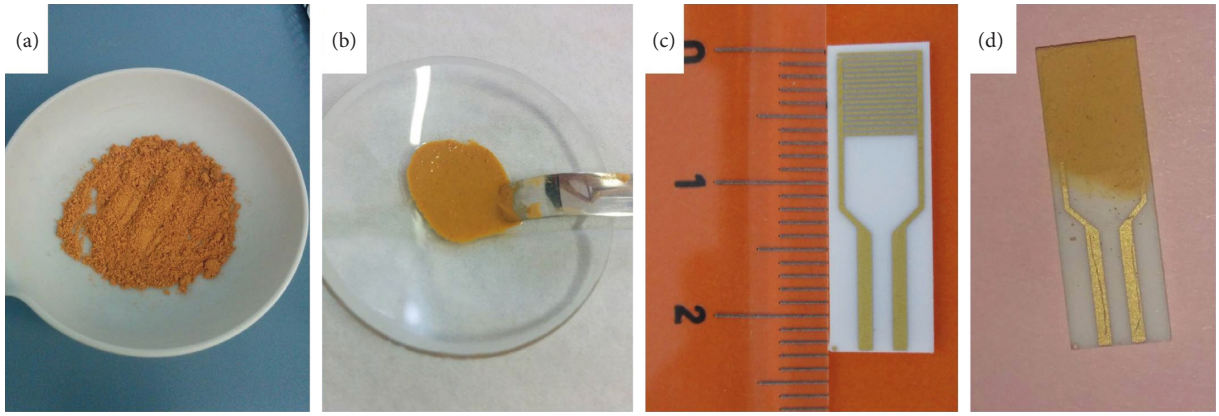

Figure 1: Preparation of sensor devices: (a) synthesized powder of perovskite sensing material; (b) paste made of powder that is dispersed into a viscous organic matrix; (c) sensing material holder with interdigitated gold electrodes that are printed on an alumina tile; (d) sensor device with calcined thin film sensing material covering the interdigitated electrodes.

The electrical resistance was measured by using a continuous method. The sensor was put into a cell made of quartz having a volume of 200 ml, which was located into a tubular oven. The resistance measurements were obtained by means of gold wires, which are connected to the sensor and go out from the cell through two sealed holes. Outside gold wires are connected by electrical cables to the multimeter Keithley2110. A gaseous solution with N_2 and CO was prepared, which are the carrier and the target gases, respectively. The electrical resistance of sensing material was recorded during and after flowing the target gas CO at 100, 150, and 200 ppm, under continuous flow of gaseous solutions of 40, 70, and 100 cm^3/min. The exposure time is not always the same, but it changes depending on the testing conditions in order to guarantee the achievement of the steady state and the dynamic equilibrium. After recovering time for the baseline, which takes few seconds, every measurement was repeated. Since every measurement is fast and perovskite oxide is highly stable sensing material, sensor drift was not recorded. Fractional sensitivity against 100, 150, and 200 ppm of CO at 300, 380, and 460°C was investigated. Every measurement was repeated, and the mean value of every experimental output data was calculated. Both picture of the flow-through reactor and schematic representation of the gas sensor testing system are shown in Figure 2.

2.5. Design of Experiments and Multiregression Analyses of Data. A full-factorial experimental design was performed in order to study the dependence of the fractional sensitivity, the normalized response rate, and the resolution ability index on the operating conditions, such as the temperature of the oven, the mass flow rate of the inlet-gas, and the concentration of the target gas. For studying fractional sensitivity and normalized response rate, a full-factorial design was used with three factors and three levels, performing twenty-seven experiments that are displayed geometrically as a body-face-edge centered cube (Figure 3), in agreement with the model matrix of the surrogate variables and the correlated experimental matrix of the real variables in Table 1.

On the other hand, for studying the resolution ability index, a full-factorial design with two factors and three levels was used, and nine experiments which are displayed geometrically as a face-edge centered square were performed (Figure 4), in agreement with the model matrix and the correlated experimental matrix in Table 2.

Nonlinear multiple regression analysis was performed in order to develop mathematical models with predictive ability, which are useful tools to define the direct and indirect effects of all experimental factors on the sensor device performance. The graphical representation of the models are the response surface diagrams, which are useful tools to define the most suitable working conditions for sensor devices, in agreement with the Quality-by-Design approach. In addition, they are useful tools for multiparametric calibration of sensor devices as well. The polynomial function proposed for fitting of the experimental data includes constant, linear, interaction, and quadratic terms:

$$Y = b_0 + b_1X_1 + b_2X_2 + b_3X_3 + b_{12}X_1X_2 + b_{13}X_1X_3 + b_{23}X_2X_3 + b_{11}X_1^2 + b_{22}X_2^2 + b_{33}X_3^2, \quad (6)$$

where Y is the response, which is either the fractional sensitivity, the normalized response rate or the resolution ability index; while the variables X_1, X_2, and X_3 are dimensionless and normalized surrogate variables, which are defined on a coded scale from −1 to +1 and represent the true experimental factors from their lowest to highest level. The coefficient b_0 is a constant, b_i and b_{ii} are related to the magnitude of the direct effects of X_i on Y, and b_{ij} is related to the magnitude of the indirect effect of X_i and X_j on Y due to their mutual interactions. The parameter p is the index for defining the statistical significance of each coefficient. The authors consider statistically significant coefficient value when $p < 0.01$.

3. Results and Discussion

3.1. Combustion Synthesis. Combustion synthesis was carried out by putting the reacting mixture on a hot plate and increasing gradually the temperature. The flame was ignited when the plate temperature was set at around 200°C. At this

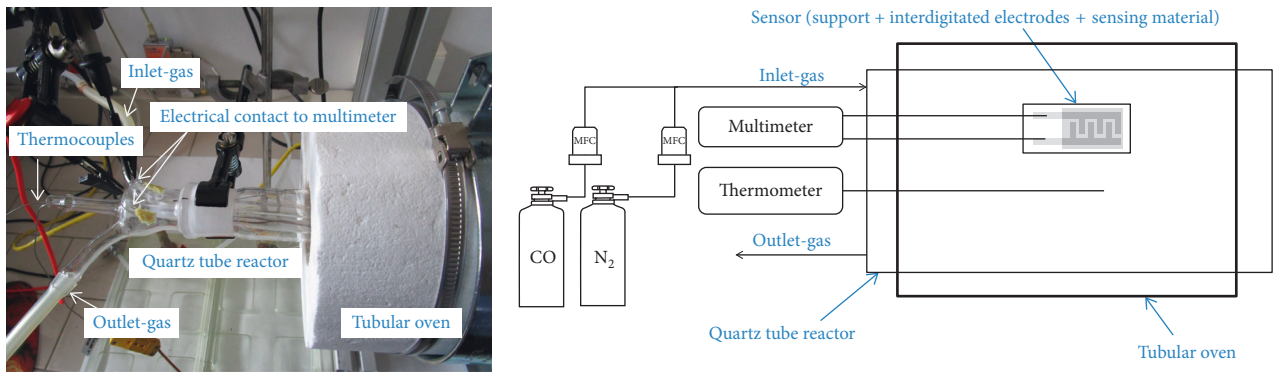

(a) (b)

FIGURE 2: Picture of the flow-through reactor and schematic representation of the gas sensor testing system.

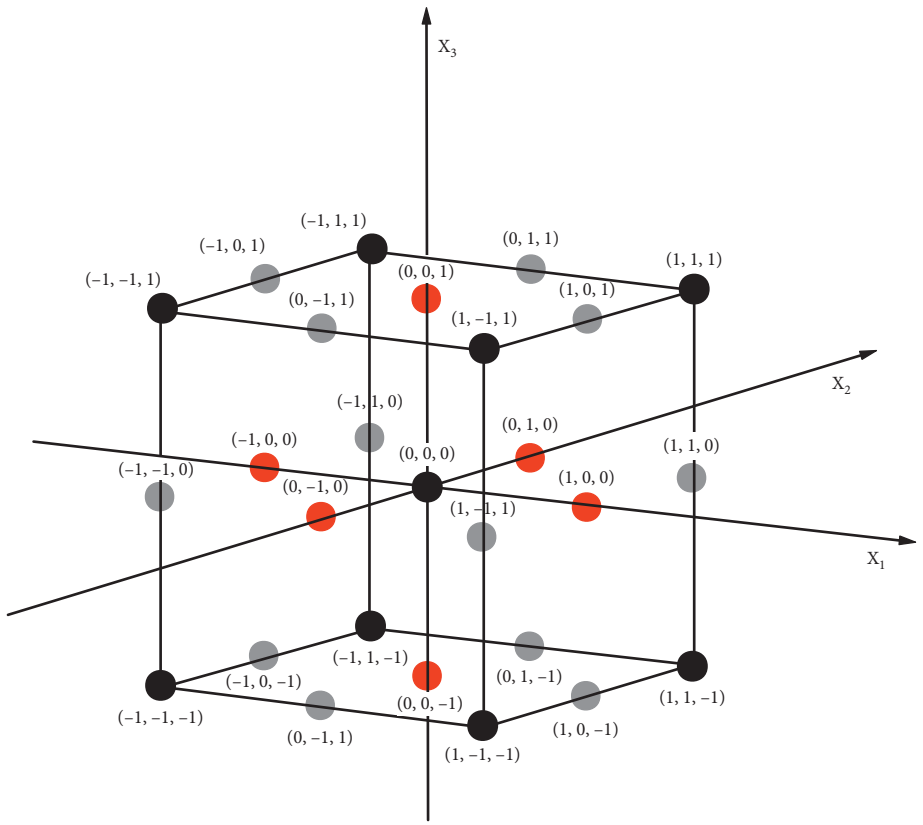

FIGURE 3: Pictorial representation of the full-factorial design with three factors and three levels for studying fractional sensitivity and normalized response rate.

temperature, the flame was ignited and the combustion synthesis process started. The heat of combustion was released almost instantaneously in a single step from a vigorous redox reaction between organic compounds and the nitrate ions:

$$5C_4H_9O^- + 5C_6H_5O_7^{3-} + 42NO_3^- \longrightarrow 62OH^- + 4H_2O + 50CO_2 + 21N_2 \quad (7)$$

In the reaction, the oxidation of NH4+ and some combustion byproducts, such as NO_x, were neglected. Since the fuel-to-oxidizer molar ratio affects the properties of the synthesized powder by controlling the flame temperature value, a fuel-to-oxidizer molar ratio, F/O, was selected, close to the stoichiometric condition. Since the fuel in the reacting solution contains both the butoxide ion and the acetate ion, it is not easy to correctly define the molar ratio between fuel and oxidizer. The problem was overcome by considering the carbon units as fuel. Since the total mole of the available carbon units is considered as the total mole of the supplied fuel, the fuel-to-oxidizer molar ratio is F/O = $(4n\text{ButO} + 6n\text{CA})/(n\text{NO}_3)$, where nButO, nCA, and $n\text{NO}_3$ are the moles of butoxide, citrate, and nitrate ions, respectively. Under this assumption, the fuel-to-oxidizer molar ratio at the stoichiometric conditions is (F/O)st = 1.19, while the

Table 1: Full-factorial design with three factors and three levels for fractional sensitivity, FS, and normalized response rate, rFS. Model matrix column shows the surrogate variables, which are X_1, X_2, and X_3; experimental matrix column shows the real variables, which are oven temperature, inlet-gas flow rate, and carbon monoxide concentration; response column shows the values of fractional sensitivity and normalized response rate, respectively.

	Model matrix			Experimental matrix			Response	
	X_1	X_2	X_3	T (°C)	φ (cm^3/min)	C (ppm)	FS (%)	rFS (% S^{-1})
ex1	−1	−1	−1	300	40	100	14.6 ± 0.6	0.08 ± 0.03
ex2	−1	−1	1	300	40	200	15.7 ± 0.6	0.14 ± 0.03
ex3	1	−1	−1	460	40	100	20.0 ± 0.6	0.11 ± 0.03
ex4	1	−1	1	460	40	200	60.2 ± 0.6	0.28 ± 0.03
ex5	−1	1	−1	300	100	100	22.7 ± 0.6	0.15 ± 0.03
ex6	−1	1	1	300	100	200	24.2 ± 0.6	0.23 ± 0.03
ex7	1	1	−1	460	100	100	19.6 ± 0.6	0.22 ± 0.03
ex8	1	1	1	460	100	200	65.9 ± 0.6	0.48 ± 0.03
ex9	−1	0	−1	300	70	100	18.3 ± 0.6	0.13 ± 0.03
ex10	−1	0	1	300	70	200	18.7 ± 0.6	0.15 ± 0.03
ex11	1	0	−1	460	70	100	33.3 ± 0.6	0.30 ± 0.03
ex12	1	0	1	460	70	200	103.4 ± 0.6	0.51 ± 0.03
ex13	0	−1	−1	380	40	100	103.7 ± 0.6	0.74 ± 0.03
ex14	0	−1	1	380	40	200	222.7 ± 0.6	1.41 ± 0.03
ex15	0	1	−1	300	100	100	204.9 ± 0.6	1.72 ± 0.03
ex16	0	1	1	460	100	200	276.8 ± 0.6	2.26 ± 0.03
ex17	−1	−1	0	300	40	150	15.2 ± 0.6	0.12 ± 0.03
ex18	1	−1	0	460	40	150	32.1 ± 0.6	0.14 ± 0.03
ex19	−1	1	0	300	100	150	21.5 ± 0.6	0.21 ± 0.03
ex20	1	1	0	460	100	150	37.8 ± 0.6	0.32 ± 0.03
ex21	0	0	−1	380	70	100	128.0 ± 0.6	0.71 ± 0.03
ex22	0	0	1	380	70	200	260.0 ± 0.6	0.91 ± 0.03
ex23	−1	0	0	300	70	150	19.4 ± 0.6	0.15 ± 0.03
ex24	1	0	0	460	70	150	67.9 ± 0.6	0.60 ± 0.03
ex25	0	−1	0	380	40	150	125.0 ± 0.6	0.81 ± 0.03
ex26	0	1	0	380	100	150	228.0 ± 0.6	1.78 ± 0.03
ex27	0	0	0	380	70	150	221.0 ± 0.6	1.80 ± 0.03

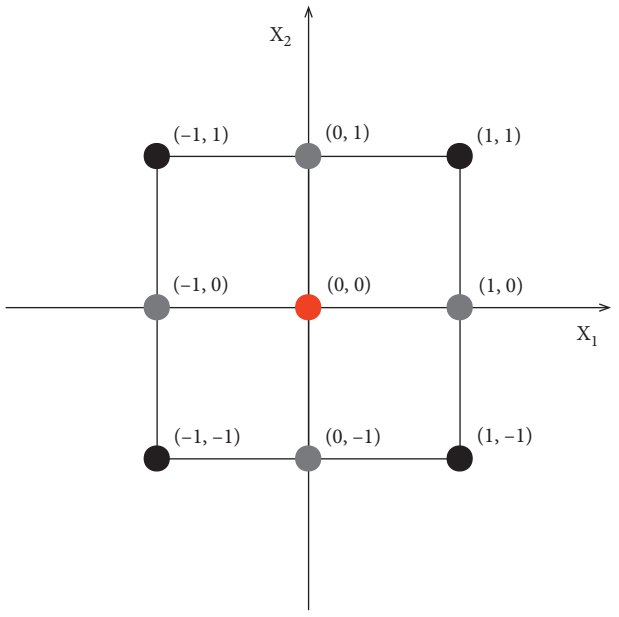

Figure 4: Pictorial representation of the full-factorial design with two factors and three levels for studying the resolution ability index.

equivalence ratio and the normalized equivalence ratio are $\phi = (F/O)/(F/O)st = 0.92$ and $\Phi = \phi/(1 + \phi) = 0.48$, respectively. However, a more reliable estimation of experimental combustion conditions is from the real number of equivalents of the fuel and the oxidizer, which is related to the amount of exchanged electrons in the redox reaction. Since every mole of butoxide and citrate loses 24 and 18 electrons, respectively, and every mole of nitrate gains 5 electrons, the fuel-to-oxidizer ratio is $F/O = (24n\text{ButO} + 18n\text{CA})/(5n\text{NO}_3)$

Table 2: Full-factorial design with two factors and three levels for the resolution ability index, RAI. Model matrix column shows the surrogate variables, which are X_1 and X_2; experimental matrix column shows the real variables, which are oven temperature and inlet-gas flow rate; response column shows the values of resolution ability index.

	Model matrix		Experimental matrix		Response
	X_1	X_2	T (°C)	φ (cm^3/min)	RAI (d.u.)
ex1	−1	1	300	100	2.2 ± 0.7
ex2	1	1	460	100	82.5 ± 0.7
ex3	−1	−1	300	40	1.9 ± 0.7
ex4	1	−1	460	40	74.8 ± 0.7
ex5	−1	0	300	70	1.1 ± 0.7
ex6	1	0	460	70	124.2 ± 0.7
ex7	0	−1	380	40	211.1 ± 0.7
ex8	0	1	380	100	126.2 ± 0.7
ex9	0	0	380	70	235.7 ± 0.7

and, consequently, the stoichiometric ratio between the fuel and the oxidizer is (F/O)st = 1, the equivalence ratio is $\phi = 0.72$, and the normalized equivalence ratio is $\Phi = 0.42$. After the ending of the flame propagation, the product of combustion reaction was a fluffy yellow powder.

If the oxidation of NH_4^+ is not neglected, the used reaction conditions result to be close to the stoichiometric conditions anyway. Indeed, in this case, since ammonium ions has to be taken into account as extra fuel, the value of fuel-to-oxidizer equivalent ratio is calculated by $F/O = (24n_{ButO} + 18n_{CA} + 3n_{NH4})/(5n_{NO3})$. Consequently, the equivalence ratio and the normalized equivalence ratio are $\phi = 1.21$ and $\Phi = 0.55$, respectively, according to following equation:

$$5C_4H_9O^- + 5C_6H_5O_7^{3-} + 5NH_4^+ + 45NO_3^- \longrightarrow 60OH^- + 15H_2O + 50CO_2 + 25N_2 \quad (8)$$

However, it is important to note that our previous work confirms that it is possible to neglect the oxidation of NH_4^+ [33].

The real flame temperature was monitored by means of a digital thermometer with two *K*-type thermocouple at two different positions inside the reacting vessel, which were close to the surface by the heater plate, in order to check the accuracy of the measurement (Figure 5). The temperature profile shows that the temperature starts from 50°C because this is not the temperature of vessel surface in contact with the heater plate, but it is the temperature of the gel at steady state condition, which is the dynamic equilibrium between the exchanged heats because the gel is heated by the hot plate and cooled by the environment at room temperature. After the initial steady state condition, the temperature increases almost instantaneously up to 800°C due to the ignition of the flame, which was obtained by setting the hot plate at 200°C.

By analyzing in depth the temperature profiles, it is possible to study the flame structure, from which it is possible to calculate the ignition temperature (Figure 6). Even though there is no universally acceptance definition, it is convenient to define the ignition temperature from the value of the second derivative of the temperature-time profile, because it is related to the acceleration of the combustion rate. Therefore, from the graph (Figure 6), it is possible to obtain the ignition temperature, which is the temperature in correspondence of the maximum value of d^2T/dt^2. The obtained ignition temperature is around 200°C, in agreement with our previous work [33]. This value is close to the required temperature value of the hot plate to start the combustion synthesis process, in agreement with Semenov model [34].

3.2. Crystal Structure Analysis. As confirmed by XRD analysis (Figure 7(a)), the synthesized powder was composed of perovskite oxide mainly because the high temperature, that was reached during the flame propagation into the reaction vessel, promotes perovskite formation. After the calcination step at 600°C in air, the powder was composed of crystalline perovskite oxide only (Figure 7(b)), because the unreacted fuels were burned, the carbonaceous matters were removed, and the crystallization processes were promoted.

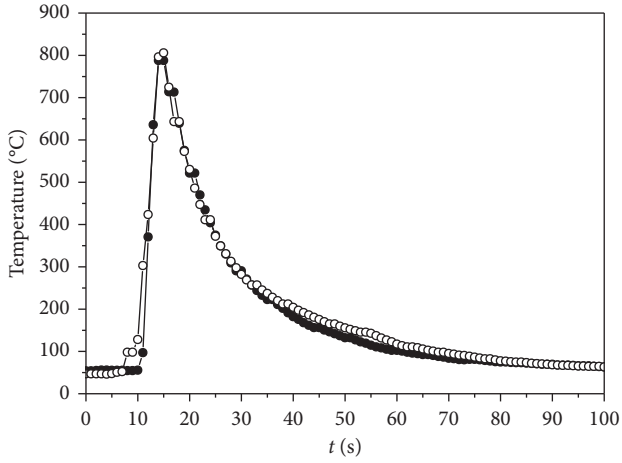

Figure 5: Temperature-time profile that was recorded during the combustion synthesis process.

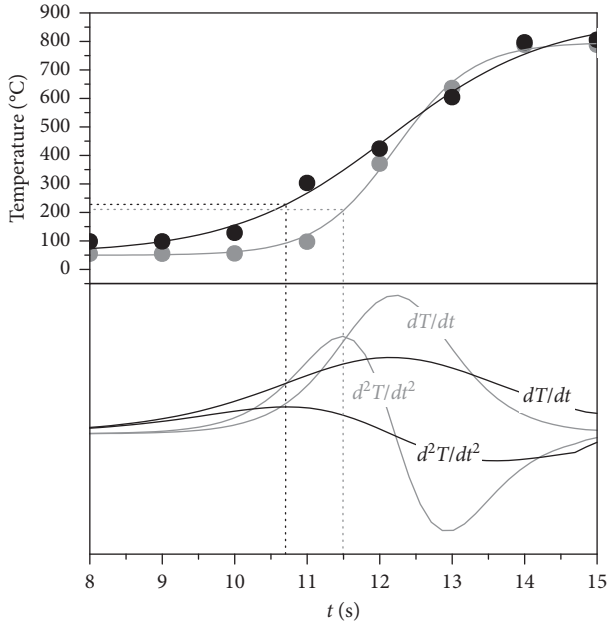

Figure 6: Temperature-time profile into the flame and the calculated first and second derivative.

The final product was $LaFe_{0.8}Ti_{0.2}O_3$ with orthorhombic crystal structure belonging to the P_{bnm} space group, as expected by taking in account the tolerance factor, *t*. Indeed, the tolerance factor, defined as $t = (R_A + R_O)/[(R_B + R_O)\sqrt{2}]$, is 1.00 and 0.95 for $LaFeO_3$ and $LaTiO_3$ respectively, because the ionic radii of La^{+3} under the coordination number 12 is 1.36 Å, while those of Fe^{+3}, Ti^{+3}, and O^{-2} under the coordination number 6 are 0.55, 0.605, and 1.40 Å, respectively [35]. Even though titanium is, in our case, inserted into perovskite structure as Ti^{+4} instead of Ti^{+3}, the mismatch between the ion radii leads to an orthorhombic system according to the tolerance factor 0.97, calculated with the ionic radius 0.605 Å of Ti^{+4}.

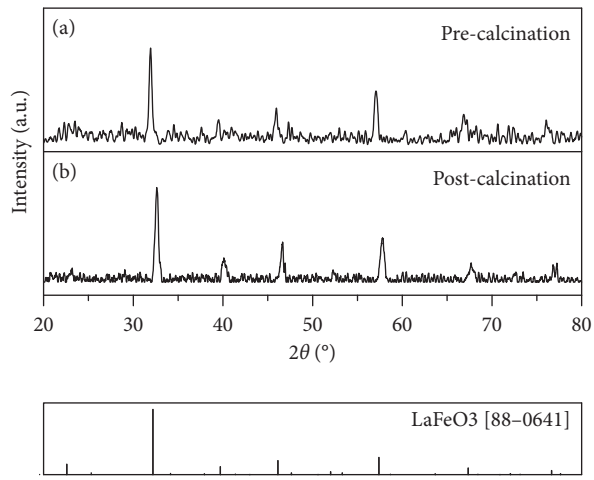

Figure 7: Patterns of XRD analyses related to the synthesized powder: (a) as obtained from the synthesis; (b) after calcination at 600°C.

3.3. Morphology Analysis. Despite the high flame temperature, the synthesized powder had high porosity and was made of particles with nanometric dimensions (Figure 8(a)) because the short combustion reaction time prevents densification and grain growth by solid-state sintering processes [36]. The solid-state sintering is a process that requires thermal energy and is divided in three overlapping stages: the initial stage is characterized by the formation of necks between particles; the intermediate stage occurs with considerable densification and interconnected pores formation; the final stage leads to the formation of isolated pores from each other. In general, the sintering rate is fast and the isolated pore stage is reached quickly, especially when powder is composed of small particle size and the sintering temperature is high. For this reason, it could be expected that combustion synthesis leads to densified material because of the high flame temperature and the combustion product nanodimensions. However, the combustion process is fast and the flame propagation along the reaction vessel takes only few seconds, as confirmed by the temperature profile, recorded during the flame propagation into the reacting vessel (Figure 5). For this reason, the synthesized powder is constituted of nanoparticles partially sintered to low-dense material with open and interconnected pores via dendritic channels.

The postcalcined powder (Figure 8(b)) keeps the high porosity and the nanoscale dimensions of the precalcined powder (Figure 8(a)), because the relative low calcination temperature and the short annealing time, leading to little grain growth with invariable distribution of relative grain sizes.

The powder is made of a network of aggregated nanometric particles with spherical morphology. The morphology of the particles does not have the expected typical cubic shape of perovskite compounds, due to the growth of thermodynamically stable [100] crystalline planes. The fast crystallization rate, that is caused by the high flame temperature of the combustion synthesis process, promotes the competition between the growth of the thermodynamically stable planes and the kinetically favored ones, that are [111] and [110]. For this reason, the powder gets the morphology kinetically promoted rather than the one thermodynamically favored.

This result confirms the reliability of autocombustion method to have useful perovskite-based sensing material because synthesized powder, that is made of small grains connected to each other with small necks, has high sensing performance. Indeed, if the size is less than twice the Debye length, a space-charge region can develop in the whole grain, allowing the achievement of maximum sensor response [27].

3.4. Resistance Profile. The resistance-time profiles of $LaFe_{0.8}Ti_{0.2}O_3$ (Figure 9) are recorded under operating conditions designed by the experimental matrix (Table 1). Every single graphic shows the resistance before, during and after flowing the target gas CO at 100, 150, and 200 ppm. In order to guarantee the achievement of the steady state and the dynamic equilibrium during all measurements, the exposure time to the target gas was not always the same, but it was changed depending on the specific operating condition, ranging from 400 to 900 seconds. After the recovering time, every measurement was repeated. Since every measurement takes few seconds and perovskite oxide is a highly stable sensing material, there was not evidence of any baseline drift.

Since the partial substitution of Fe^{+3} with Ti^{+4} in $LaFe_{0.8}Ti_{0.2}O_3$ promotes the oxygen vacancies refilling process, reaction (2), in order to neutralize the positive change excess, the hole concentration is increased and, consequently, it is expected that $LaFe_{0.8}Ti_{0.2}O_3$ exhibits *p*-type semiconductor behavior under testing conditions.

Since the resistance increases when CO flows inside the testing cell, it is confirmed that $LaFe_{0.8}Ti_{0.2}O_3$ acts as a *p*-type semiconductor. Indeed, the interaction of reducing gas, such as CO, removes atomic oxygen from the metal oxide and produces free electrons. These latter ones reduce electronic conductivity of *p*-type semiconductor because they neutralize part of preexistent holes, the main charge carrier. The interaction between reducing gas and the metal oxide occurs either via surface process, affecting the amount of adsorbed oxygen by reaction (9), or via bulk process, leading to stoichiometry changes by reaction (10).

$$CO + O^{-}_{ad} \longrightarrow CO_2 + e^{-} \quad (9)$$

$$CO + O^{X}_{O} \longrightarrow CO_2 + V_{\ddot{O}} + e^{-} \quad (10)$$

In the reactions (9) and (10), O^{-}_{ad} is the most reactive form of ionosorbed oxygen, O^{X}_{O} is lattice oxygen with neutral charge and $V_{\ddot{O}}$ is oxygen vacancy with one positive charge. Since experimental resistance changes are fast compared to expected diffusion rate of the oxygen vacancies in the solid, it is possible to claim that the conductivity changes are due to surface interactions, rather than the bulk stoichiometry changes. In addition, experimental data show a complete recovery of the conductivity after flowing CO, confirming that the interaction does not lead to persistent changes that are conversely produced by bulk processes.

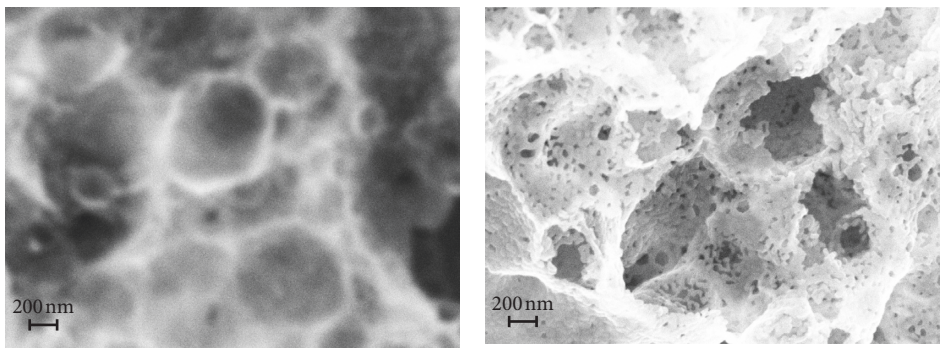

Figure 8: Images of SEM analyses related to the synthesized powder: (a) as obtained from the synthesis; (b) after calcination at 600°C.

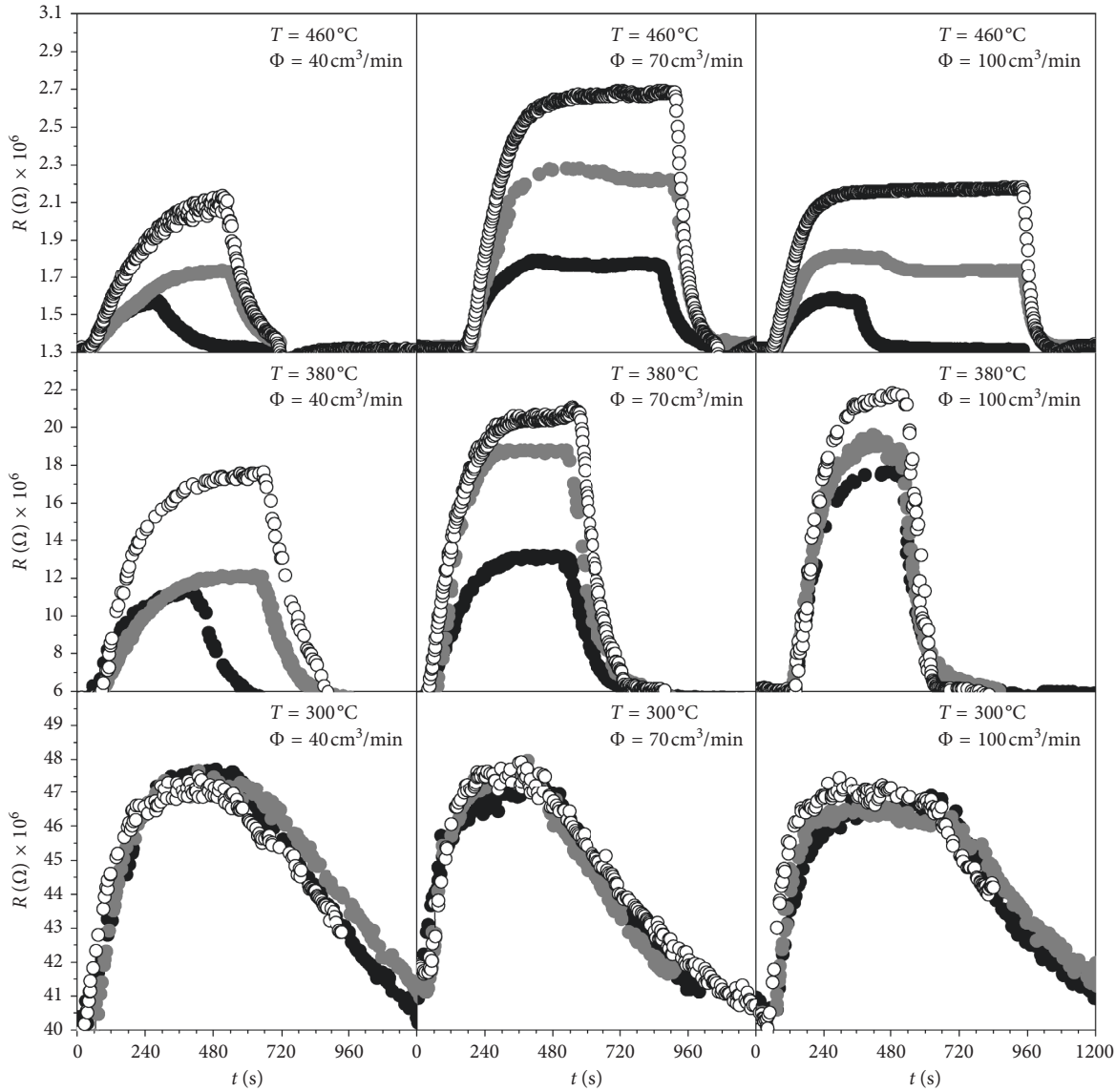

Figure 9: Electrical resistance changes due to 100, 150, and 200 ppm of carbon monoxide, that are represented with a black, gray, and white circle, respectively, when gas sensor device is under different operating conditions: temperature spans the values from 300 to 380 and 460°C; inlet-gas flow rate spans the values from 40 to 70 and 100 cm^3/min.

In addition, there is no evidence of any resistance drift, although the sensing material is exposed to reducing agents at high temperature, that could promote the lattice collapse to new phases. The complete reversibility of the target gas effects confirms the absence of bulk reactions.

3.5. Performance Analyses. The graphics in Figure 10 show the fractional sensitivity profile over time. Since fractional sensitivity is a normalized parameter, it is possible to study easily the fractional sensitivity of the sensor device under different experimental conditions by comparing directly the graphs having ordinate axes with the same linear scale. At low temperature, the fractional sensitivity is quite low (Figure 10) even though it recorded experimental resistance changes (Figure 9).

Performance analysis is shown in Figures 11 and 12, where it is, respectively, reported the fractional sensitivity and the normalized response rate against the concentration of carbon monoxide at different values of gas flow rate and temperature. As expected, both the fractional sensitivity and the normalized response rate increase monotonically with increasing the concentration of CO because the interaction between the target gas and the metal oxide surface, reaction (9), is shifted toward the production of electrons, according to the principle of Le Chatelier, and its forward rate is increased, according to law of mass action. However, the dependence of the fractional sensitivity and the normalized response rate on carbon monoxide concentration is not significant at low temperature.

In addition, it is possible to note that both the fractional sensitivity and the normalized response rate do not increase monotonically with increasing the temperature because their maximum values are obtained at intermediate temperatures due to its contrary effects on the physical adsorption of CO and on the kinetic of the reaction involving adsorbed CO and superficial oxygen, reaction (9). In general, physical adsorption of gaseous molecules on a solid surface is a spontaneous process ($\Delta G < 0$), leading to a more ordered system ($\Delta S < 0$). For this reason, spontaneous physical adsorption is an exothermic process ($\Delta H < 0$) according with the Gibbs free energy function ($\Delta G = \Delta H - T\Delta S$). Hence, CO physical adsorption is favored at low temperatures in agreement with the Van't Hoff equation. On the other hand, the rate of reaction (9) is promoted at high temperature, according to Arrhenius equation. Consequently, there is an optimum temperature at which the fractional sensitivity and the normalized response have got maximum values [37].

Finally, the experimental data in Figures 11 and 12 show that the inlet-gas flow rate affects both the fractional sensitivity and the normalized response. Indeed, high flow rate promotes reaction (9) because of the large amount of available target gas per unit of time on the perovskite surface. In addition, high flow rate generates turbulence in the gaseous solution leading to reduction of the diffusion boundary layer thickness and promoting, consequently, the diffusion of CO toward the perovskite surface. However, the dependence of the fractional sensitivity and the normalized response on the flow rate is not significant at low temperature because of the low reactivity of available target gas regardless of their amount.

For performing a multiple-criteria decision analysis, it is graphed fractional sensitivity against normalized response rate (Figure 13). The best sensing performances, that means the highest fractional sensitivity and the highest normalized response rate, are obtained with working conditions planned in the experiment ex16 (Table 1) that applies the intermediate value of temperature and the maximum value of flow rate and CO concentration: $T = 380^{\circ}\text{C}$, $\varphi = 100\,\text{cm}^3/\text{min}$, and $C = 200\,\text{ppm}$, respectively. It is interesting to note the direct correlation between FS and rFS, confirming that the normalized parameters are useful for comparing the performance of sensor device under different experimental conditions. This would not have been possible, if the author had used resistance changes as a sensitive parameter and response time or the rate of resistance changes as a kinetic parameter.

3.6. Posttest Analyses. In order to be able to compare the sensing performances under different operating conditions, the sensing material has to keep unaltered its chemical and physical properties [38]. In other words, it is necessary that the target gas does not irreversibly react with the perovskite leading to a stable new material and the aging process does not modify the material morphology [39]. Even though perovskite shows a reversible sensing activity against carbon monoxide (Figure 9), the authors have performed posttest analyses (Figure 14) in order to confirm the chemical and morphological stability of perovskite. XRD analysis (Figure 14(a)) confirms the absence of any new stable reduced phase occurred from the reduction of perovskite by carbon monoxide. SEM pictures (Figure 14(b)) confirms the absence of mass densification due to sintering processes, occurring under prolonged exposure to high temperatures.

3.7. Mathematical Models. Since sensor testing procedure involves multiple factors, that affect directly and indirectly sensing performances, chemometric analysis was applied. This analytical approach includes two successive steps: planning experiments in agreement with the full-factorial three level design; performing multivariate analysis of collected data in order to develop mathematical models. The investigated range of each factor was as follows: temperature from 300 to 460°C; inlet-gas flow rate from 40 to 100 cm^3/min; and CO concentration from 100 to 200 ppm. The polynomial function proposed for the multiple regression analyses, equation (4), includes linear-terms for studying direct effects of the factors, cross terms for discovering eventual indirect effects due to the mutual interaction between factors, and square-terms to provide a more appreciable fitting of the mathematical models.

Since the trend and the value of leverage is the same for all mathematical models, it makes no sense to show all leverage plots related to the fractional sensitivity, the normalized response rate and the resolution ability index. Therefore, it is shown only the dependence on temperature

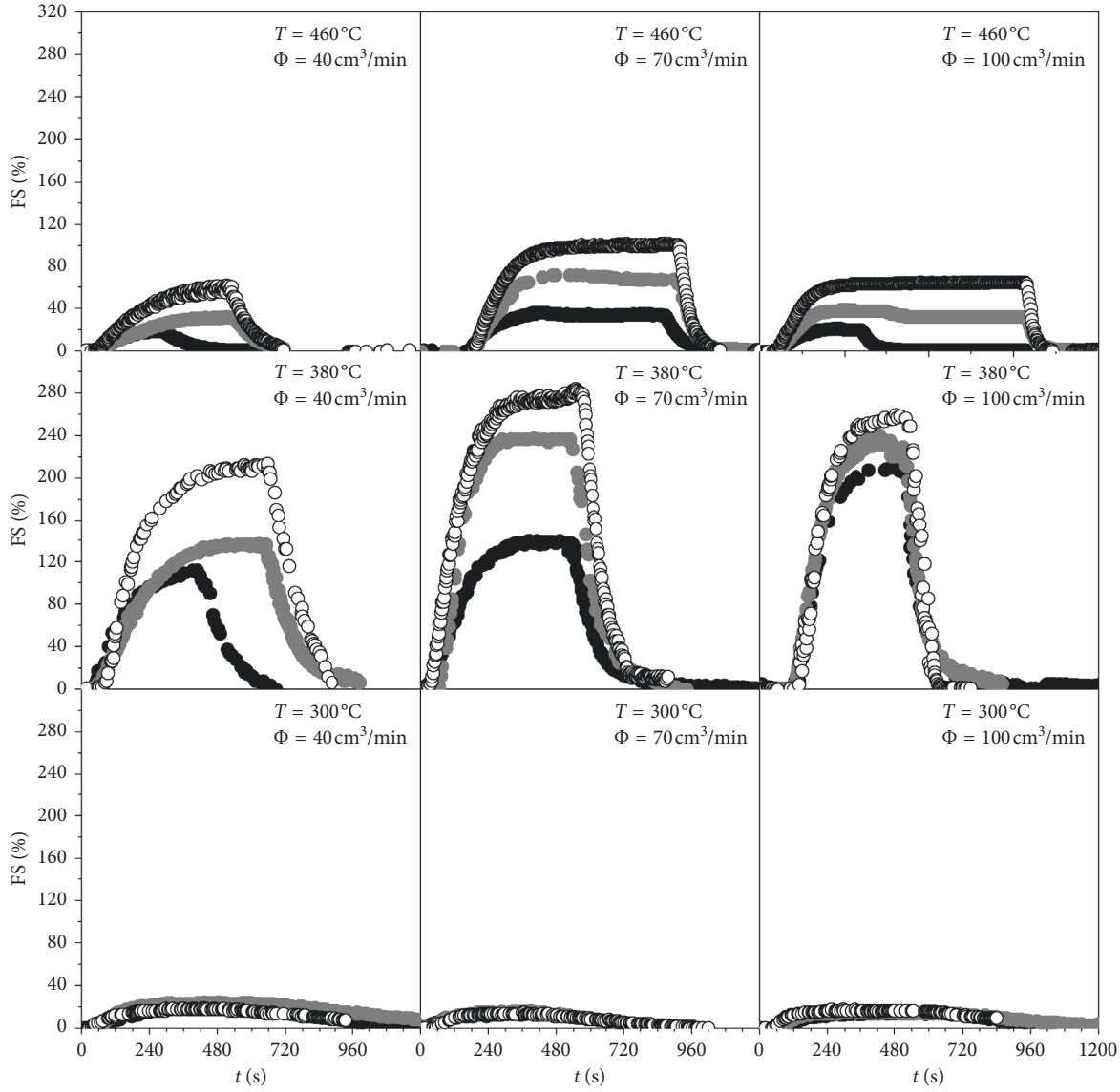

Figure 10: Fractional sensitivity time profile against 100, 150, and 200 ppm of carbon monoxide, that are represented with a black, gray, and white circle, respectively, when gas sensor device is under different operating conditions: temperature spans the values from 300 to 380 and 460°C; inlet-gas flow rate spans the values from 40 to 70 and 100 cm^3/min.

and concentration of the leverage related to the fractional sensitivity for the mathematical model calculated by full-factorial design with three factors (Figure 15). Since the leverage computed in every point of the experimental domain is much lower than unity, the precision of the predicted response obtained by the computed multiple regression model is much better than that of every experimental data: indeed, the result of multiplying leverage value by the experimental variance corresponds to the variance of the predicted value in that point [40].

3.7.1. Full-Factorial Design for Fractional Sensitivity and Normalized Response Rate Analysis. It was investigated the direct and indirect effects of temperature (T), inlet-gas flow rate (φ) and carbon monoxide concentration (C) on both fractional sensitivity (FS), and the normalized response rate (rFS) by performing twenty-seven measurements under the experimental operating conditions planned in Table 1.

The fitting polynomial function proposed for the regression analyses has the surrogate factors X_1, X_2, and X_3, that are coded scale values representing the real factors T, φ, and C, respectively, while the response Y is either FS or rFS.

Since the bar charts related to the fractional sensitivity and the normalized response rate, (Figures 16(a) and 16(b)), show that the coefficients b_1, b_2, and b_3 of both mathematical models are statistically significant, it is reasonable to claim that all T, φ, and C affect significantly both FS and rFS because they directly affect the interaction between the target gas and the sensing material.

Temperature affects directly the reaction rate of (9) in agreement with the Arrhenius law and CO adsorption in

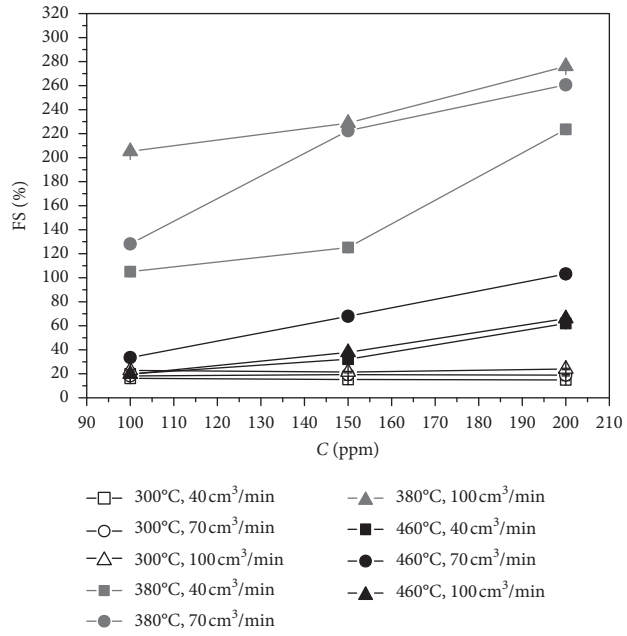

Figure 11: Graphical representation of the fractional sensitivity against the concentration of carbon monoxide at different values of inlet-gas flow rate and temperature.

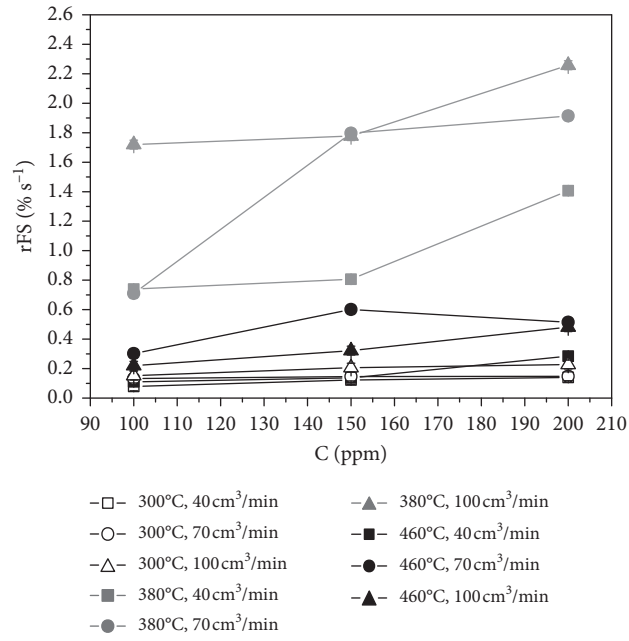

Figure 12: Graphical representation of the normalized response rate against the concentration of carbon monoxide at different values of inlet-gas flow rate and temperature.

agreement with Van't Hoff law, as already discussed. In addition, it affects indirectly the reaction rate because of its effects on the CO diffusivity along the boundary layer, that provides the available amount of carbon monoxide to the metal oxide surface.

Gas flow rate affects not only the turbulence close to the sensing surface with repercussions on the diffusion boundary layer thickness, but also the contact time between the target gas and sensing material with repercussions on the penetration depth of the target gas into the porous sensing material. In other words, inlet-gas flow rate has effects on the real interacting surface area and, consequently, on the kinetic of the reaction (9), affecting rFS, and on the magnitude of the electrical resistance changes, affecting FS.

The gas concentrations have effects on the chemical equilibrium composition of reaction (9) by Le Chatelier's principle, affecting the amount of reacted CO and, consequently, the magnitude of FS. Also, it affects the kinetics of surface chemical reactions in agreement with the law of mass action and, consequently, rFS depends on target gas concentrations. Finally, it impacts the diffusion of the target gas toward the sensing surface along the diffusion boundary layer, affecting both FS and rFS.

The cross term b_{13} in Figure 16(a) is statistically significant in the mathematical model because carbon monoxide concentration affects the temperature effects on the fractional sensitivity and vice-versa. This occurs because both the carbon monoxide concentration and the temperature take an active part in the same key steps of the sensing process, that are the carbon monoxide diffusion along the boundary layer, adsorption on the metal oxide surface, and the reaction with the active site of the sensing material. However, these interaction effects are very low under the investigated operating conditions. Figure 17(a) shows that the relationship between the fractional sensitivity and the concentration depends significantly on temperature because the slope of the linear function describing their relationship changes from 0.2 to 0.4 and 0.6% ppm^{-1} when the temperature increases from 300 to 360 and 460°C, respectively; indeed, the contour plot shows that FS changes from 20 to 40% at 300°C, from 180 to 220% at 380°C and from 40 to 100% at 460°C, when the C is changed from 100 to 200 ppm.

On the other hand, the cross term b_{13} in Figure 16(b) is not statistically significant because CO concentration and temperature does not significantly affect each other in the mathematical model related to the normalized response rate. Indeed, Figure 18(a) shows that the relationship between the normalized response rate and the concentration does not depend significantly on temperature because their linear relationship does not change with the temperature, and it has a constant slope of $4{\cdot}10^{-3}$% $s^{-1}{\cdot}ppm^{-1}$; in effect, the contour plot shows that the rFS change from 0 to 0.4% s^{-1} at 300°C, from 1.2 to 1.6% s^{-1} at 380°C and from 0.2 to 0.6% s^{-1} at 460°C, when C is changed from 100 to 200 ppm. However, at 300 and 460°C the response rate keeps at low levels due to the kinetic inhibition of the reaction of target gaseous with sensing materials under low temperature and the thermodynamic inhibition against the physical adsorption process under high temperature; while at intermediate temperature the response rate is quite high.

The cross terms b_{23} in Figures 16(a) and 16(b) are not statistically significant in both mathematical models because inlet-gas flow rate does not significantly alter the effects of carbon monoxide concentration on both fractional sensitivity and the normalized response. Indeed, Figure 17(b) shows that the relationship between the fractional sensitivity

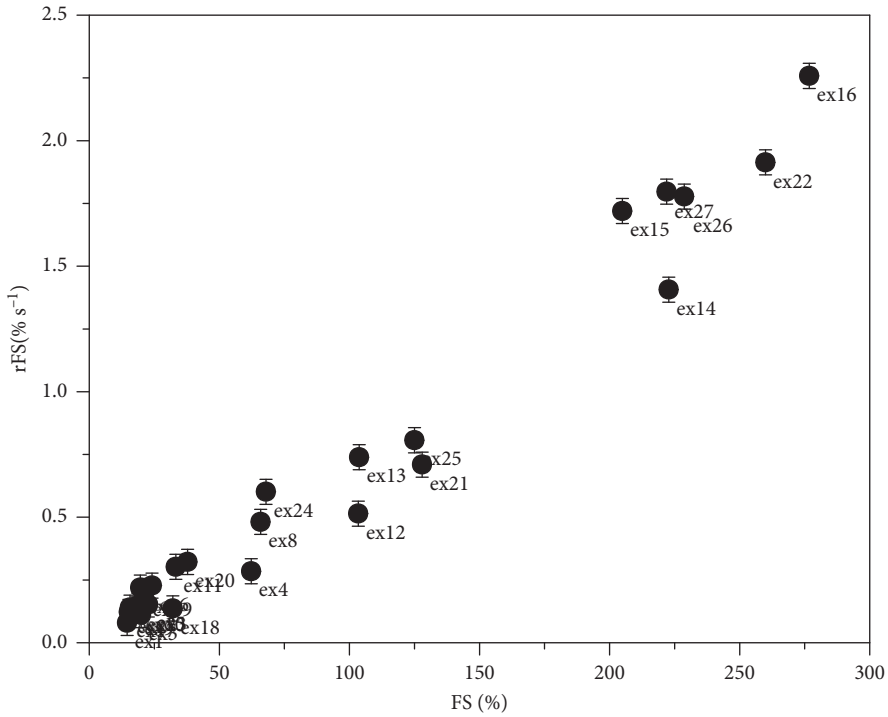

Figure 13: Graphical representation of the fractional sensitivity against the normalized response rate for the multiple-criteria decision analysis.

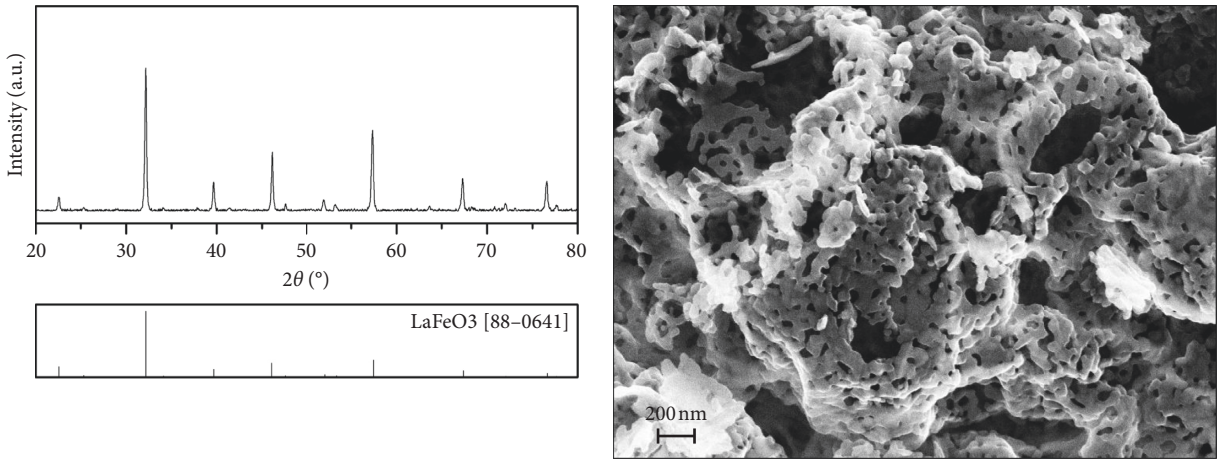

Figure 14: Posttest analyses of sensing materials: (a) XRD; (b) SEM.

and the concentration does not depend significantly on the value of inlet-gas flow rate because the slope of the linear function describing their linear relationship is 0.5% ppm^{-1} at whatever temperature: the contour plot shows that FS changes from 150 to 200%, from 180 to 230%, and from 180 to 230% at 300, 380, and 460°C, respectively. One extra information obtained from this data is the quadratic dependence between the fractional sensitivity and the inlet-gas flow rate because FS reaches the plateau value of 180 and 230% when carbon monoxide concentration is 100 and 200 ppm, respectively. In the same way, Figure 18(b) shows that the linear relationship between the normalized response rate and the concentration does not depend significantly on the inlet-gas flow rate because the slope is $5{\cdot}10^{-3}$% s$^{-1}{\cdot}$ppm^{-1} at whatever φ value.

The cross terms b_{12} in Figures 16(a) and 16(b) are not statistically significant because inlet-gas flow rate does not significantly compromise the effects of carbon monoxide concentration on both fractional sensitivity and the normalized response. Indeed, Figure 17(c) shows that the relationship between the fractional sensitivity and the inlet-gas flow rate does not depend significantly on the temperature because FS increases by 40 units when the inlet-gas flow rate increase from 40 to 100 cm$^3{\cdot}$min at whatever temperature; in

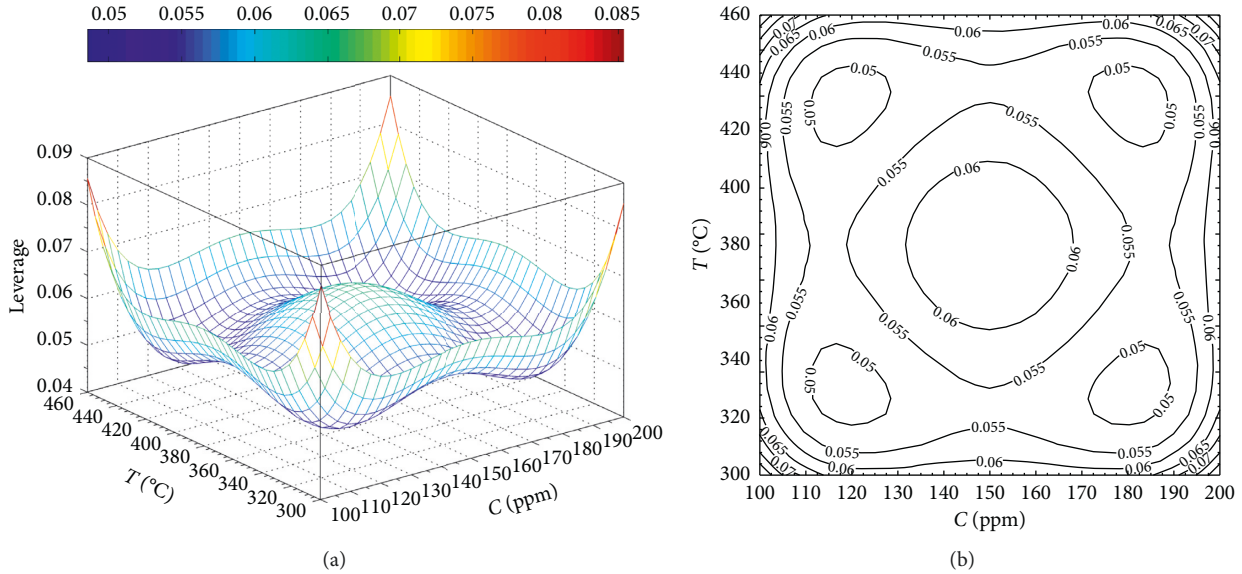

Figure 15: Leverage plot related to full-factorial design for fractional sensitivity, showing the dependence on temperature and carbon monoxide concentration.

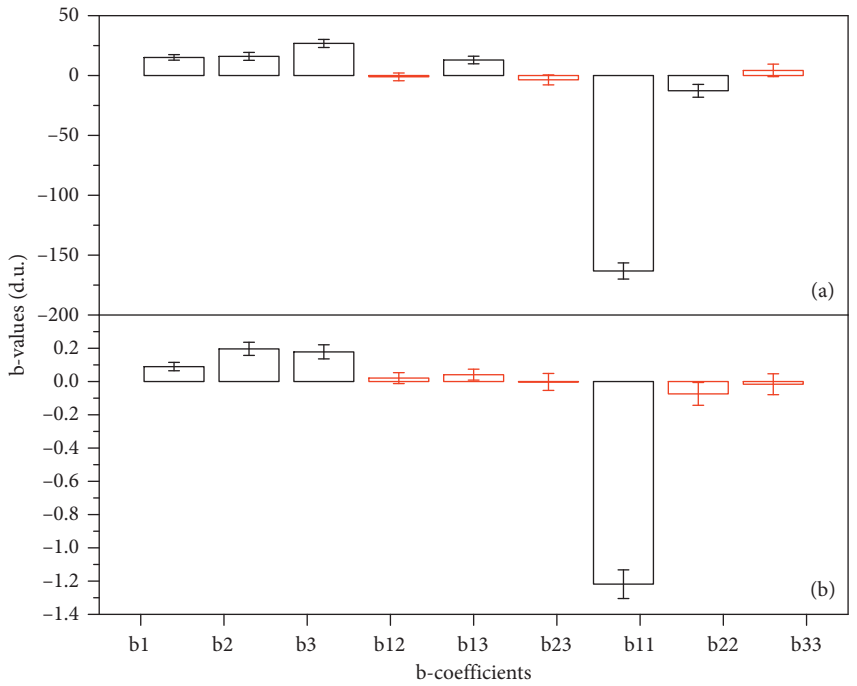

Figure 16: Bar chart of b-coefficient values and their standard deviations, where the red bars are coefficient values that are not statistically significant: (a) coefficients related to the mathematical model for fractional sensitivity; (b) coefficients related to the mathematical model for normalized response rate.

fact, the contour plot shows that FS changes from 0 to 40%, from 160 to 200%, and from 20 to 60% at 300, 380, and 460°C, respectively. Similarly, Figure 18(c) shows that the linear relationship between the normalized response rate and the inlet-gas flow rate does not depend significantly on the temperature because the slope is $4{\cdot}10^{-3}\%\,s^{-1}{\cdot}ppm^{-1}$ at whatever T value.

The term b_{11} is statistically significant in both models, Figures 16(a) and 16(b), because the dependence of the fractional sensitivity and the normalized response rate on the temperature is not linear but quadratic. Indeed, the temperature has two different conflicting effects on the sensor performance. The large value of the coefficient b11 indicates the importance of the conflicting role that the temperature has. Indeed, the temperature strongly inhibits the physical adsorption of CO, but strongly promotes the reaction (9), at the same time. For this reason, Figures 17(a) and 18(a) show bell-shaped response surfaces, from which it

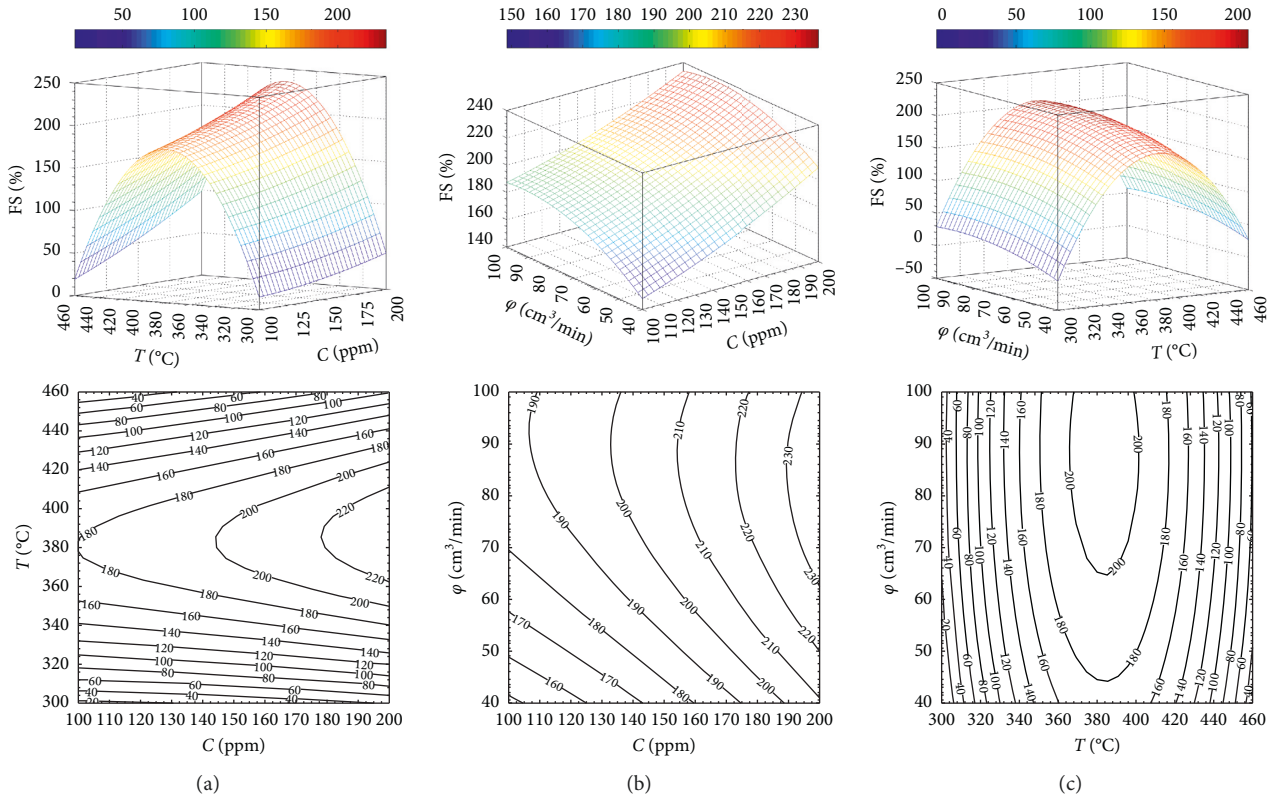

FIGURE 17: Response surface and counter plot related to the polynomial function describing the operating conditions effects on the fractional sensitivity: (a) effects of temperature and carbon monoxide concentration, when inlet-gas flow rate is 70 cm^3/min; (b) effects of inlet-gas flow rate and carbon monoxide concentration, when temperature is 380°C; (c) effects of inlet-gas flow rate and temperature, when carbon monoxide concentration is 150 ppm.

can easily be seen that the best fractional sensitivity and normalized response rate are obtained under intermediate temperature.

The term b_{22} is statistically significant in the model related to the fractional sensitivity (Figure 16(a)) because it does not increase indefinitely with increasing the inlet-gas flow rate, but it rises asymptotically towards a plateau value, as shown in the response surface (Figures 17(b) and 17(c)). Indeed, with high values of inlet-gas flow rate, the process begins chemical controlled and the amount of available target gas on the perovskite surface is no more dependent on it. In general, the fate of the target gas in the sensing process includes seven steps: the diffusion towards the external surface of the sensing thin layer, the internal diffusion into the pores, the adsorption on the sensing material surface, the chemical reaction leading to surface electrical resistance change, the desorption of the products, and the subsequent internal and external diffusion of the products. In particular, solid porous sensing materials based on metal oxide semiconductor detect a target gas by its chemical reactions with superficial oxygens, O^-_{ad}, as described in the reaction (9). Since the chemical reaction occurs on the metal oxide surface consuming the reagents, the concentration of the reagents on the surface is different from that in the bulk, leading to a concentration gradient into the boundary layer. The reagent supply to the surface occurs by the gas diffusion along the boundary layer, that depends on the partial pressures, the molecular diffusion coefficient, and the thickness of the boundary layer. By increasing the inlet-gas flow rate, the turbulence increases and, consequently, the boundary layer thickness decreases promoting the diffusion of the target gas toward the surface. In this case, the slow step of the sensing process is the diffusion and, consequently, the sensing process is faster when the inlet-gas flow rate is higher. However, when the inlet-gas is too high, the slow step is the chemical reaction and, consequently, the sensitivity does not change with further increase in inlet-gas flow rate. Indeed, even though the reaction rate is actually affected by the inlet-gas flow rate because it controls the supply of target gas per unit of time on the surface, the defined number of superficial active sites for sensing reactions limits the effect of inlet-gas flow rate. Therefore, the excessive increase in inlet-gas flow rate leads to the transition from the diffusional regime, that is due to the mass-transfer limitations, toward the chemical regime, where the slow step, that controls the whole sensing process, is the reaction (9) [41–43].

On the other hand, the coefficient b_{22} is not statistically significant in the model related to the normalized response rate because it did not show quadratic dependence under the investigate operating conditions.

In addition, the coefficient b_{33} is not statistically significant in both models (Figures 16(a) and 16(b)), because

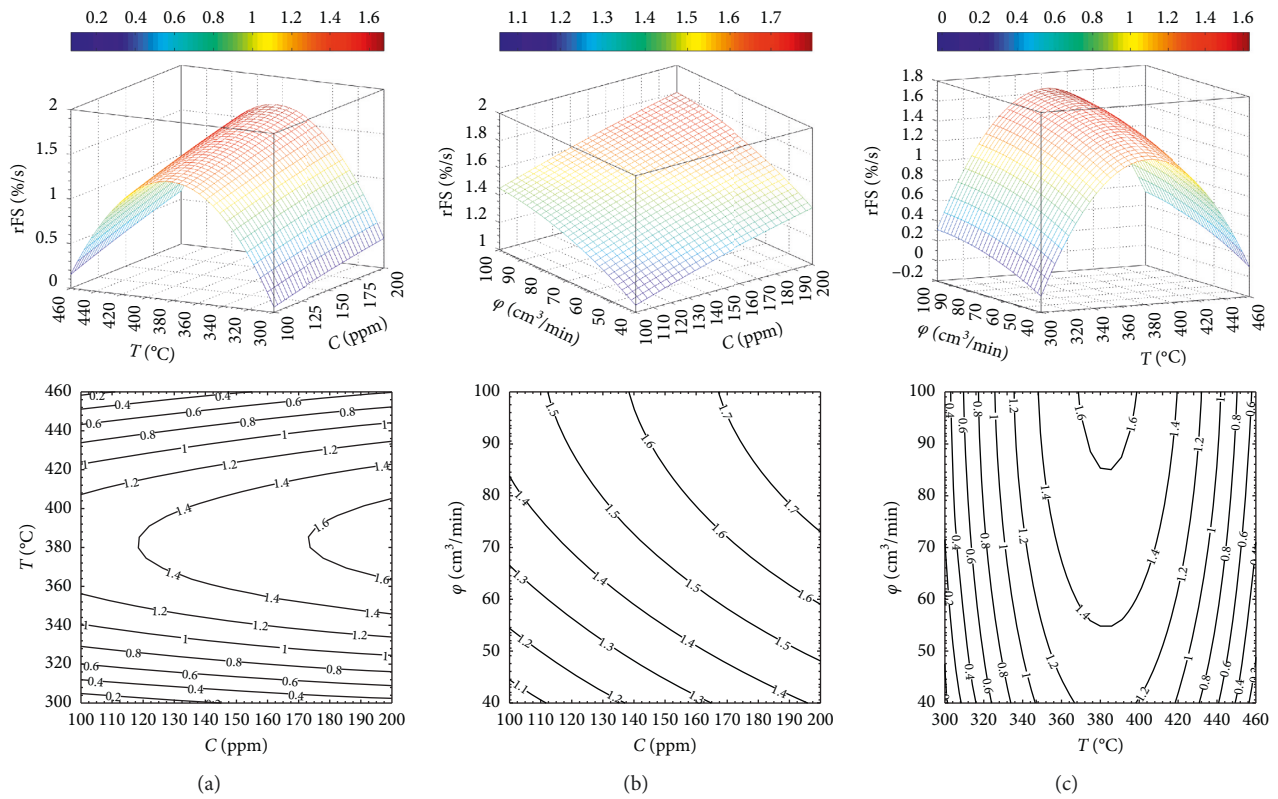

FIGURE 18: Response surface and counter plot related to the polynomial function describing the operating conditions effects on the normalized response rate: (a) effects of temperature and carbon monoxide concentration, when inlet-gas flow rate is 70 cm^3/min; (b) effects of inlet-gas flow rate and carbon monoxide concentration, when temperature is 380°C; (c) effects of inlet-gas flow rate and temperature, when carbon monoxide concentration is 150 ppm.

the concentrations of carbon monoxide are within the linearity range of the calibration curve.

3.7.2. Full-Factorial Design for Resolution Ability Index Analysis. It was investigated the direct and indirect effects of temperature and inlet-gas flow rate on the resolution ability index by performing nine experiments, as indicated in Table 2. The fitting polynomial function has the surrogate factors X_1 and X_2, that are related to the real factors T and φ, respectively; while the response Y is the sensor resolution ability index, RAI. The model matrix with the surrogate variables, the experimental matrix with the real variables and the measured responses are shown in Table 2.

Since the bar chart (Figure 19), shows that b_1 and b_2 are statistically significant, both the temperature and the inlet-gas flow rate affect significantly the resolution ability index. In addition, the dependence between the resolution ability index and the two studied factors is quadratic, as confirmed by the significant values of the coefficients b_{11} and b_{22}. However, the b_{12} value is not statistically significant, it means that there is not any significant mutual interaction between the temperature and the inlet-gas flow rate within the investigated experimental domain.

Three-dimensional response surface and the corresponding contour plot (Figure 20), show the bell shape

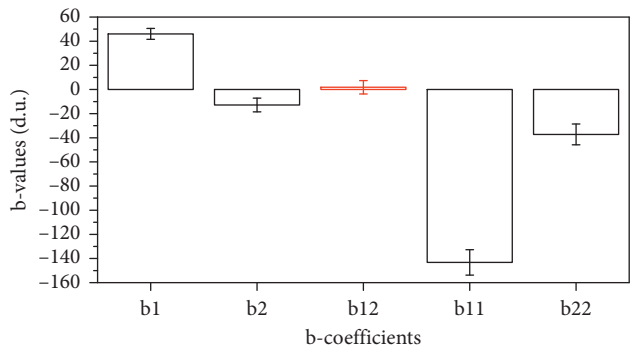

FIGURE 19: Bar chart of b-coefficient values with standard deviations related to full-factorial design with two factors for studying the sensor resolution ability index. The red bars are coefficient values that are not statistically significant.

trend of the resolution ability index against both temperature and flow rate, spanning the values from 0 to 120. It is possible to predict that the optimum experimental condition in order to have the highest resolution ability index is when both the temperature and the inlet-gas flow rate have intermediate values. Indeed, under lower and higher values, the interaction between the target gas and the sensing surface is either kinetically or thermodynamically inhibited: temperature affects the gas adsorption on sensing surface and the chemical reaction (9); inlet-gas flow rate

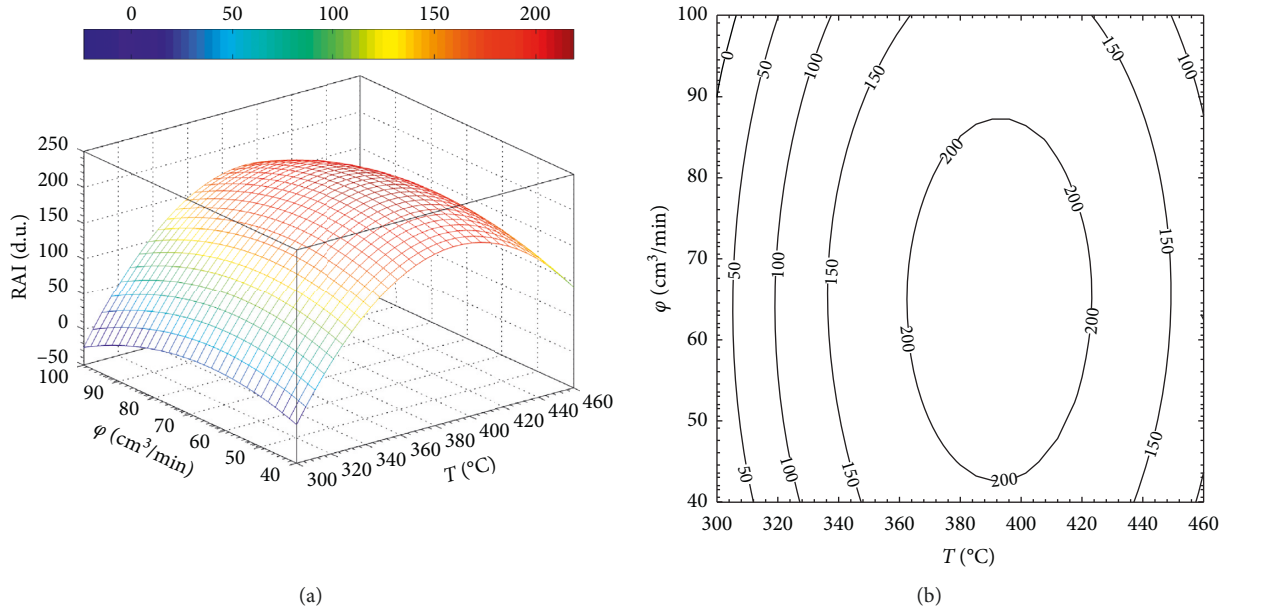

FIGURE 20: Response surface and counter plot related to the polynomial function describing the effect of both the inlet-gas flow rate and the temperature on the resolution ability index.

affects the gas diffusion to sensing surface and the contact time.

The worst condition, that is related to a null resolution ability index, is observed when temperature is low and the flow rate is high because the interaction rate at the interface level is low and the contact time is short.

By overlapping in Figure 21 the contour plots related to the fractional sensitivity and the resolution ability index as function of temperature and gas flow rate, that are in Figures 17(c) and 20 respectively, it is possible to know the best working condition of the sensor. The best sensor performance is obtained under intermediate values of both temperature and inlet-gas flow rate in a restrict range within the investigated experimental conditions, that is the gray zone in Figure 21.

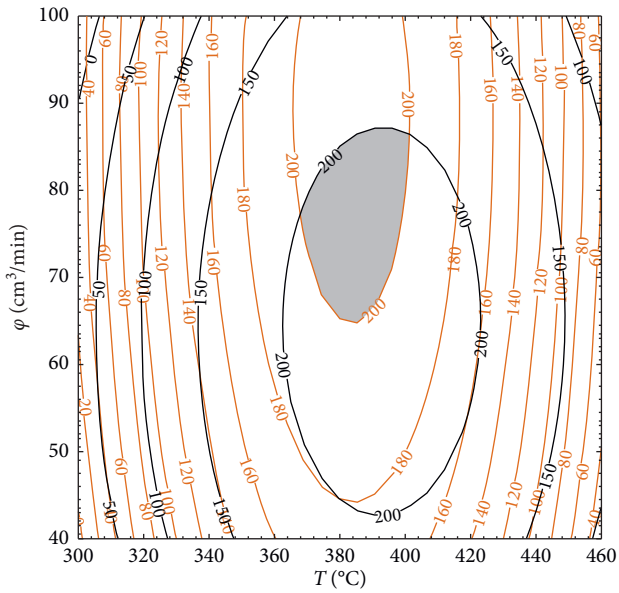

FIGURE 21: Overlapping of contour plots related to the fractional sensitivity (red lines) and resolution ability index (black lines), that both describe the effect of inlet-gas flow rate and temperature.

4. Conclusion

Perovskite oxides $LaFe_{0.8}Ti_{0.2}O_3$ with orthorhombic crystalline structure was synthesized by the autocombustion method, that has led to powder made of a single phase, a material with homogenous composition and zero-dimension particles with high porosity. From systematic studies, that apply Quality-by-Design principles, it was optimized the working conditions for CO sensor devises made of a thin film of $LaFe_{0.8}Ti_{0.2}O_3$ sensing material deposited on a interdigitated gold electrodes over ceramic substrate. The output of the multiple regression analyses defined the direct and indirect effects of temperature, inlet-gas flow rate, and carbon monoxide concentration on sensor performances. In accordance with the mathematical models, all investigated experimental factors affect the fractional sensitivity and normalized response rate of the sensor device. The concentration of carbon monoxide and the temperature affect each other, leading to a global effect on the fractional sensitivity because both the mass-transfer diffusion along the boundary layer and the reaction of the target gas on the sensing surface are affected by the CO concentration and temperature in the same time. In addition, temperature and inlet-gas flow rate affect resolution ability index of the sensor device without any significant mutual interaction.

Finally, it is possible to claim that the best working conditions are with intermedia temperature and inlet-gas flow rate. Fractional sensitivity, normalized response rate, and resolution ability index do not increase monotonically

with increasing the temperature; indeed, target gas physical adsorption on sensing surface is promoted at low temperature, while the reaction rate between the target gas and the sensing material is promoted at high temperature. In addition, inlet-gas flow rate has a nonlinear effect on sensor performances because the interaction between target gas and sensing surface is kinetically inhibited under both low and high values of inlet-gas flow rate; indeed, the target gas diffusion towards sensing surface is promoted at high flow rate, while the contact time between target gas and sensing material is promoted at low flow rate.

In addition, it is important to note that the mathematical model related to the effects of CO concentration, inlet-gas flow rate, and temperature on the fractional sensitivity can be used as multicalibration curve. The usage of a response surface as calibration surface overcame problems related to unexpected and unwanted changes fluctuation of operating condition, such as inlet-gas flow rate and temperature.

Data Availability

The data used to support the findings of this study are included within the article.

Conflicts of Interest

The authors declare no conflicts of interest.

Authors' Contributions

Fabio Zaza supervised the experimental activity and wrote the manuscript; Fabio Zaza and Vanessa Pallozzi synthetized, characterized, and tested the sensing material; Emanuele Serra provided technical support for SEM analyses.

Acknowledgments

The project was supported by ENEA-Casaccia Research Centre.

References

[1] A. Deptula, M. Milkowska, W. Lada et al., "Vitrification of nuclear wastes by complex sol-gel process," *Advanced Materials Research*, vol. 518–523, pp. 3216–3220, 2012.

[2] F. Zaza, M. Pasquali, E. Simonetti, C. Paoletti, and A. Dell'Era, "Innovative nanomaterials for fuel cells fed with biogas," *Nuovo Cimento della Societa Italiana di Fisica C*, vol. 36, no. 2, pp. 73–81, 2013.

[3] V. Pallozzi, A. DiCarlo, F. Zaza, M. Villarini, M. Carlini, and E. Bocci, "Perovskite sensing materials for syngas composition monitoring and biomass gasifier numerical model validation: a preliminary approach," *AIP Conference Proceedings*, vol. 1749, p. 020002, 2015.

[4] V. Pallozzi, F. Zaza, E. Serra, A. DiCarlo, M. Villarini, and M. Carlini, "Gas sensors for sustainable and safe bioenergy production from an integrated gasification-FC system," in *Proceedings of 21st World Hydrogen Energy Conference*, vol. 126681, pp. 893-894, Zaragoza, Spain, June 2016.

[5] P. K. Sekhar, E. L. Brosha, R. Mukundan, and F. Garzon, "Chemical sensors for environmental monitoring and homeland security," *The Electrochemical Society Interface*, vol. 19, no. 4, pp. 35–40, 2010.

[6] A. Hulanicki, S. Glab, and F. Ingman, "Chemical sensors: definitions and classification," *Pure and Applied Chemistry*, vol. 63, no. 9, pp. 1247–1250, 1991.

[7] S. Capone, A. Forleo, L. Francioso et al., "Solid state gas sensors: state of the art and future activities," *Journal of Optoelectronics and Advanced Materials*, vol. 5, no. 5, pp. 1335–1348, 2003.

[8] M. Batzill and U. Diebold, "The surface and materials science of tin oxide," *Progress in Surface Science*, vol. 79, no. 2–4, pp. 47–154, 2005.

[9] N. Barsan, M. Schweizer-Berberich, and W. Gopel, "Fundamental and practical aspects in the design of nanoscaled SnO2 gas sensors: a status report," *Fresenius' Journal of Analytical Chemistry*, vol. 365, no. 4, pp. 287–304, 1999.

[10] W. Göpel and K. D. Schierbaum, "SnO2 sensors: current status and future prospects," *Sensors and Actuators B: Chemical*, vol. 26, no. 1-3, pp. 1–12, 1995.

[11] J. W. Orton and M. J. Powell, "The Hall effect in polycrystalline and powdered semiconductors," *Reports on Progress in Physics*, vol. 43, no. 11, pp. 1263–1307, 2000.

[12] A. Rothschild and Y. Komem, "The effect of grain size on the sensitivity of nanocrystalline metal-oxide gas sensors," *Journal of Applied Physics*, vol. 95, no. 11, pp. 6374–6380, 2004.

[13] F. Zaza, S. Frangini, J. Leoncini et al., "Temperature-independent sensors based on perovskite-type oxides," in *Proceedings of AIP Conference*, vol. 1603, pp. 53–61, Rome, Italy, June 2014.

[14] F. Zaza, G. Orio, E. Serra, F. Caprioli, and M. Pasquali, "Low-temperature capacitive sensor based on perovskite oxides," in *Proceedings of AIP Conference*, vol. 1667, Rome, Italy, June 2015.

[15] V. Pallozzi, F. Zaza, A. Di Carlo, E. Bocci, and M. Carlini, "Gas sensors for sustainable and safe integrated gasification-FC system," *International Journal of Hydrogen Energy*, vol. 42, no. 49, pp. 29606–29619, 2017.

[16] Nova Science Publishers, "The microwave dielectric properties of Ca[(Li1/3A2/3)1-xMx]O3-δ [A=Nb, Ta and M=Ti, Zr, Sn] dielectric ceramics," in *Perovskites: Structure, Properties and Uses*, M. Borowski, Ed., Nova Science Publishers Inc., New York NY, USA, 2010.

[17] D. Ielmini and R. Waser, *Resistive Switching: from Fundamentals of Nanoionic Redox Processes to Memristive Device Applications*, John Wiley & Sons, Hoboken, NJ, USA, 2016.

[18] P. J. Gellings and H. J. M. Bouwmeester, *The CRC Handbook of Solid State Electrochemistry*, CRC Press, Boca Raton, FL, USA, 1996.

[19] M. J. Madou and S. R. Morrison, *Chemical Sensing with Solid State Device*, Academic Press, Cambridge, MA, USA, 1989.

[20] T. Ishihara, *Perovskite Oxide for Solid Oxide Fuel Cells*, Springer, Berlin, Germany, 2009.

[21] S. Li, L. Jing, W. Fu, L. Yang, B. Xin, and H. Fu, "Photoinduced charge property of nanosized perovskite-type LaFeO3 and its relationships with photocatalytic activity under visible irradiation," *Materials Research Bulletin*, vol. 42, no. 2, pp. 203–212, 2007.

[22] A. A. Saad, W. Khan, P. Dhiman, A. H. Naqvi, and M. Singh, "Structural, optical and magnetic properties of perovskite (La1-xSrx)(Fe1-xNix)O3, (x = 0.0, 0.1 & 0. 2) nanoparticles," *Electronic Materials Letters*, vol. 9, no. 1, pp. 77–81, 2013.

[23] K. Li, D. Wang, F. Wu, T. Xie, and T. Li, "Surface electronic states and photovoltage gas-sensitive characters of nanocrystalline LaFeO3," *Materials Chemistry and Physics*, vol. 64, no. 3, pp. 269–272, 2000.

[24] J. Mizusaki, T. Samoto, W. R. Cannon, and H. K. Bowen, "Electronic conductivity, seebeck coefficient, and defect structure of LaFe03," *Journal of the American Ceramic Society*, vol. 65, no. 8, pp. 363–368, 1982.

[25] T. Wolfrant and S. Ellialtioglu, *Elecronic and Optical Properties of d-Band Perovskites*, Cambridge University Press, Cambridge, UK, 2006.

[26] F. Zaza, V. Pallozzi, E. Serra, and M. Pasquali, *Combustion synthesis of LaFeO3 sensing nanomaterial* in *Proceedings of AIP Conference*, vol. 1667, Rome, Italy, June 2015.

[27] G. Korotcenkov, "The role of morphology and crystallographic structure of metal oxides in response of conductometric-type gas sensors," *Materials Science and Engineering: R: Reports*, vol. 61, no. 1–6, pp. 1–39, 2008.

[28] V. E. Bochenkov and G. B. Sergeev, "Sensitivity, selectivity, and stability of gas-sensitivity metal-oxide nanostructures," in *Metal Oxide Nanostructures and their applications*, A. Umar and Y.-B. Hahn, Eds., pp. 31–52, American Scientific Publishers, Valencia, FL, USA, 2010.

[29] M. J. McGrath, C. NiScanaill, and D. Nafus, *Sensor Technologies: Healthcare, Wellness and Environmental Applications*, Apress, New York City, NY, USA, 2013.

[30] K. Arshak, E. Moore, G. M. Lyons, J. Harris, and S. Clifford, "A review of gas sensors employed in electronic nose applications," *Sensor Review*, vol. 24, no. 2, pp. 181–198, 2004.

[31] R. Khler, "International vocabulary of metrology–basic and general concepts and associated terms (VIM)," in *Transverse Disciplines in Metrology*, Vol. 200, JCGM, Västerås, Sweden, 2012.

[32] D. A. Skoog, D. M. West, F. J. Holler, and S. R. Crouch, *Fundamentals of Analytical Chemistry*, Brooks/Cole, Boston, MA, USA, 1995.

[33] F. Zaza, G. Orio, and E. Serra, "Quality by design approach for SrTiO3 perovskite nanomaterials synthesis," *Journal of Materials Science*, vol. 51, no. 21, pp. 9649–9668, 2016.

[34] I. Glassman and R. Yetter, *Combustion*, Academic Press, Cambridge, MA, USA, 2008.

[35] R. D. Shannon, "Revised effective ionic radii and systematic studies of interatomic distances in halides and chalcogenides," *Acta Crystallographica Section A*, vol. 32, no. 5, pp. 751–767, 1976.

[36] S. J. L. Kang, *Sintering: Densification, Grain Growth, and Microstructure*, Elsevier, New York City, NY, USA, 2005.

[37] M. Jaroniec and R. Madey, *Physical Adsorption on Heterogeneous Solids*, Elsevier, New York City, NY, USA, 1988.

[38] T. Inoue, N. Seki, J.-i. Kamimae, K. Eguchi, and H. Arai, "The conduction mechanism and defect structure of acceptor- and donor-doped SrTiO3," *Solid State Ionics*, vol. 48, no. 3-4, pp. 283–288, 1991.

[39] G. Korotcenkov, "Gas response control through structural and chemical modification of metal oxide films: state of the art and approaches," *Sensors and Actuators, B: Chemical*, vol. 107, no. 1, pp. 209–232, 2005.

[40] R. Leardi, "Experimental design in chemistry: a tutorial," *Analytica Chimica Acta*, vol. 652, no. 1-2, pp. 161–172, 2009.

[41] E. Santacesaria, "Kinetics and transport phenomena," *Catalysis Today*, vol. 34, no. 3-4, pp. 393–400, 1997.

[42] E. Santacesaria, "Kinetics and transport phenomena in heterogeneous gas-solid and gas-liquid-solid systems," *Catalysis Today*, vol. 34, no. 3-4, pp. 411–420, 1997.

[43] M. DiGiulio, D. Manno, G. Micocci, A. Serra, and A. Tepore, "Gas-sensing properties of sputtered thin films of tungsten oxide," *Journal of Physics D: Applied Physics*, vol. 30, no. 23, pp. 3211–3215, 1997.